Geochemistry, Geophysics, Geosystems®

AGU ADVANCING EARTH AND SPACE SCIENCE

RESEARCH ARTICLE
10.1029/2022GC010368

Rock Magnetic Signatures of Hydrothermal Mineralization in the Trans-Atlantic Geotraverse (TAG) Hydrothermal Field

Shishun Wang[1] and **Liao Chang**[1,2]

[1]Laboratory of Orogenic Belts and Crustal Evolution, School of Earth and Space Sciences, Peking University, Beijing, China, [2]Laboratory for Marine Geology, Qingdao National Laboratory for Marine Science and Technology, Qingdao, China

Abstract The Ocean Drilling Program Leg 158 drill holes from the Trans-Atlantic Geotraverse hydrothermal field are investigated to understand the rock magnetic signatures of hydrothermal mineralization. A composite columnar section has been constructed through hole correlation to understand the stratigraphic variation of magnetomineralogy within the stockwork. Isothermal remanent magnetization components unmixing, first-order reversal curve diagrams, low-temperature magnetic signatures, and electron microscopic analyses disclose magnetic minerals of disparate occurrences related to predominating hydrothermal mineralization reactions in three broad zones: For basaltic basements, serpentinization of olivine phenocrysts during preliminary hydrothermal alteration produces magnetite, in addition to primary titanomagnetite; Chloritized and silicified zone samples contain relict titanomagnetite and exsolved magnetite that survived hydrothermal dissolution; Anhydrite and sulfide zone samples are dominated by magnetite and hematite, likely from oxidation of polymetallic sulfides due to exposure in oxidative seafloor environments during drilling. Our findings suggest that seafloor oxidation potentially modifies the magnetic properties of polymetallic sulfides in hydrothermal deposits, which applies to magnetic tomography of sophisticated subseafloor vent structures and prospecting seafloor massive sulfides (SMS) deposits therein. Meanwhile, we alert future deep-sea mining that drilling may promote physicochemical alteration of SMS deposits, causing environmental risks. The established magnetic signatures ultimately contribute to understanding the in situ geological preservation of SMS deposits and optimizing exploitation procedures in the future.

Plain Language Summary Seawater can be leaked into the oceanic crust along mid-ocean ridges and produce black smoker fluids through various chemical reactions. Such reactions leave traces in ocean crust: primary minerals are destroyed (hydrothermal alteration) and new minerals form (hydrothermal mineralization). Magnetic methods provide a powerful tool to explore seafloor active or inactive black smokers. However, it is less efficient when focusing on particular newly-formed minerals, that is, polymetallic sulfides with a resource potential, because their magnetic contrast with other minerals is poorly understood. Here, we investigate black smoker rock samples from the Trans-Atlantic Geotraverse field and find that the magnetic properties of these polymetallic sulfides may be affected by the seafloor oxidizing environment during drilling or geological preservation. This finding suggests that the physical and chemical properties of polymetallic sulfides can be modified by external disturbance, which should be taken seriously in future seafloor mining to minimize any potential environmental damages.

Key Points:

- A composite columnar section is constructed to show stratigraphic variations of magnetic parameters in the Trans-Atlantic Geotraverse (TAG) stockwork
- Hydrothermal alteration of the TAG basalts involves serpentinization of olivine phenocrysts, producing magnetite
- Oxidation modifies the magnetic properties of the hydrothermally-mineralized TAG seafloor massive sulfides

Supporting Information:

Supporting Information may be found in the online version of this article.

Correspondence to:

L. Chang,
liao.chang@pku.edu.cn

Citation:

Wang, S., & Chang, L. (2022). Rock magnetic signatures of hydrothermal mineralization in the Trans-Atlantic Geotraverse (TAG) hydrothermal field. *Geochemistry, Geophysics, Geosystems*, *23*, e2022GC010368. https://doi.org/10.1029/2022GC010368

Received 25 JAN 2022
Accepted 12 APR 2022

Author Contributions:

Conceptualization: Shishun Wang, Liao Chang
Data curation: Shishun Wang, Liao Chang
Formal analysis: Shishun Wang
Funding acquisition: Liao Chang
Investigation: Shishun Wang, Liao Chang
Methodology: Shishun Wang, Liao Chang
Project Administration: Liao Chang
Resources: Shishun Wang, Liao Chang
Supervision: Liao Chang
Validation: Shishun Wang

1. Introduction

High-temperature hydrothermal circulation hosted by mid-ocean ridge basalt (MORB) is essential for understanding lithosphere-hydrosphere interactions (German & Seyfried, 2014; Schwarzenbach & Steele-MacInnis, 2020; Tivey, 2007) and producing seafloor massive sulfides (SMS) with resource potential (Hannington et al., 2011). Magnetic surveying has been playing a key role in locating both active and inactive seafloor high-temperature vent fields (e.g., Gehrmann et al., 2019; Tivey & Johnson, 2002) and probing their subseafloor structures (e.g., Caratori Totini et al., 2016; Galley et al., 2021). The primary mechanisms of hydrothermal-related negative magnetic anomalies are the progressive dissolution of primary titanomagnetite during hydrothermal alteration of MORB (Wang et al., 2020, 2021) and the formation of hydrothermal deposits with low magnetization (Szitkar et al., 2014). Therefore, magnetic analyses of in situ stratigraphic rock samples from hydrothermal fields are essential for linking magnetic surveying with geological observations.

Visualization: Shishun Wang
Writing – original draft: Shishun Wang
Writing – review & editing: Shishun Wang, Liao Chang

The Trans-Atlantic Geotraverse (TAG) hydrothermal field (Figure 1a; Rona et al., 1986), located in the rift valley of the Mid-Atlantic Ridge near latitude 26°08'N, is one of the best-studied hydrothermal fields to date (Humphris et al., 2015). Ocean Drilling Program (ODP) Leg 158 delineated that fluid-rock reactions beneath the TAG active mound include coupled MORB hydrothermal alteration (i.e., chloritization and silicification) and repeated precipitation of anhydrite and polymetallic sulfides as hydrothermal deposits (Humphris et al., 1995, 2015). Post-cruise rock magnetic analyses identified minor magnetite and pyrrhotite in the TAG hydrothermal deposits (Zhao et al., 1998), preserving weak but complex remanent magnetization of chemical origins. However, detailed magnetomineralogy and magnetic property variations among different hydrothermal products in TAG were not established by Zhao et al. (1998). Consequently, although the low concentration of magnetic minerals within the stockwork explains the reduced crustal magnetization in the TAG active mound (e.g., Gehrmann et al., 2019; Tivey et al., 1993), utilizing magnetic surveying data for sophisticated subsurface stockwork geometry inversion and tonnage estimation of SMS deposits remain challenging (e.g., Galley et al., 2021; Szitkar et al., 2021).

In this study, based on the findings of Zhao et al. (1998), we revisit the rock magnetic properties of samples recovered during ODP Leg 158. A composite columnar section from multiple holes is constructed to demonstrate the stratigraphic variations of magnetic parameters with different lithology zonations. Through comprehensive rock magnetic and electron microscopic analyses, we show that magnetic minerals in SMS deposits and fully-altered MORBs can have different occurrences, despite their similar bulk magnetic parameters. We also provide evidence that the magnetic minerals in SMS deposits may form through the oxidation of polymetallic sulfides in suboceanic conditions.

2. Materials and Methods

2.1. Samples

In September—November 1994, ODP Leg 158 drilled 17 holes into the TAG active mound within a radius of 200 m (Site 957) to understand its internal structures (Humphris et al., 1996). Drilling recovered materials down to 125.7 mbsf (Hole 957E), producing a composite transection of the TAG mound, which from bottom to top can be divided into basalt zone, chloritized zone, silicified zone, anhydrite zone, and sulfide zone (Humphris et al., 1995, 1996). The chloritized, silicified, anhydrite, and sulfide zones define the stockwork. Detailed lithological descriptions can be found in Humphris et al. (1996) and are briefly summarized here. Hydrothermal alteration dominates the chloritized and silicified zone, where basalt, chloritized basaltic breccia, silicified wallrock breccia, and pyrite-silica breccia represent a progressive alteration pathway (Honnorez et al., 1998; Figure S1 and Text S1 in Supporting Information S1). The presence of anhydrite and sulfide marks hydrothermal mineralization, which prevails as veins and breccias in anhydrite (pyrite-silica-anhydrite breccias and pyrite-anhydrite breccias) and sulfide zones (massive pyrite or pyrite breccias), though some sulfide and anhydrite veins are also identified in chloritized and silicified zone samples (Knott et al., 1998; Figure S1 and Text S1 in Supporting Information S1).

Representative lithologies of different zonations were sampled (~10 cm^3 unoriented chips) from 10 holes (Figure 1a) to avoid biases from spatial inhomogeneity. A total of 55 samples were collected. Sample density was measured using a solid densitometer. As Holes 957E-G have the deepest penetration and most complete zonation (Humphris et al., 1996), a composite columnar section is constructed through lithostratigraphic correlations with Holes 957E-G (Figure S2 in Supporting Information S1). Five basalt samples from Hole 957M are exceptions because they represent underlying basement, and thus they are extended below Hole 957E-G (Figure 1b). It is worth noting that there are some uncertainties in the exact zone boundaries due to the overall low recovery (13.3% on average) of the drill holes (Humphris et al., 1996). Consequently, we only use this columnar section to demonstrate rock magnetic property variations of different zonations with no implications for actual stockwork structures.

2.2. Rock Magnetic Measurements

Three ~0.5 g chips were cut from each sample for magnetic measurements and the results were averaged. Powders were also prepared for specific magnetic measurements. The volume of chips and powders was calculated from their actual weight and density, enabling magnetization data to be volume-normalized. Susceptibility was measured with a 200 A/m applied field and 976 Hz operating frequency using an AGICO MFK-1FA Kappabridge

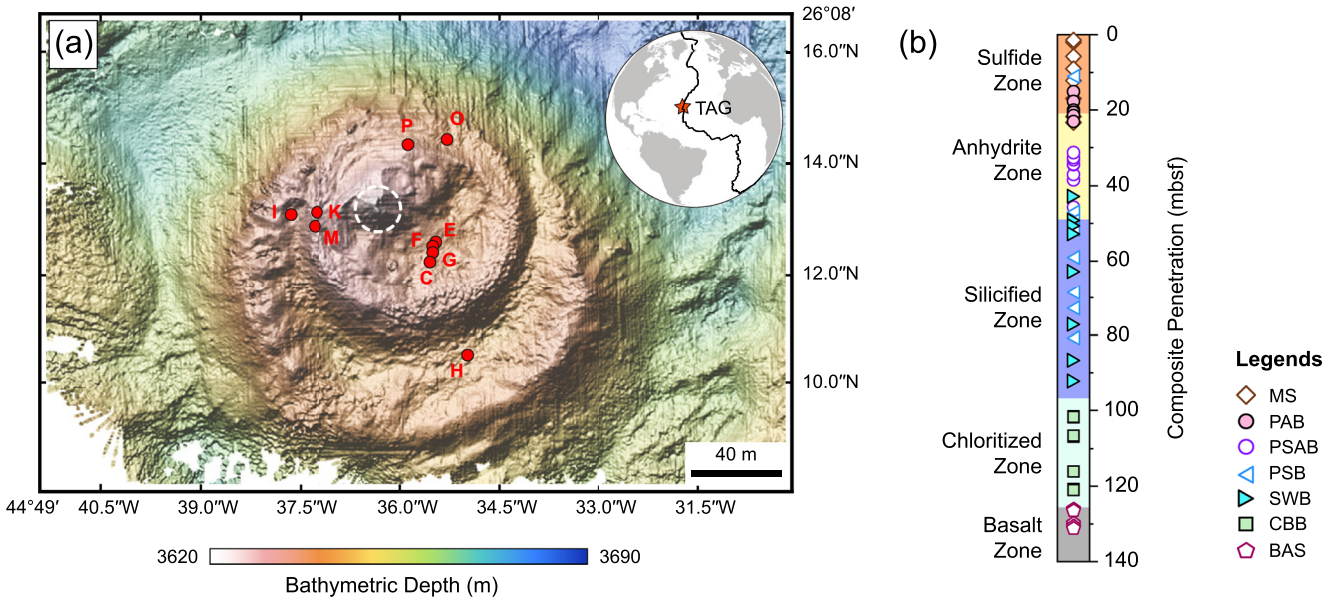

Figure 1. Bathymetry and drill holes of the active mound in the Trans-Atlantic Geotraverse (TAG) hydrothermal field. (a) High-resolution bathymetry map of the active mound in the TAG field (Roman & Singh, 2007). Inset gives a global view of the location of the TAG field. The white dashed circle locates the active vent. Red dots indicate Ocean Drilling Program Leg 158 Site 957 drill holes (Humphris et al., 1996), and only those from which samples were collected for this study are shown. (b) A composite columnar section constructed through correlations to Holes 957E-G (Figure S2 in Supporting Information S1). Based on shipboard descriptions (Humphris et al., 1996), samples with different lithologies are indicated. MS = massive sulfides (breccia), PAB = pyrite-anhydrite breccia, PSAB = pyrite-silica-anhydrite breccia, PSB = pyrite-silica breccia, SWB = silicified wallrock breccia, CBB = chloritized basaltic breccia, BAS = basalt.

at the Paleomagnetism Laboratory, Peking University (PKU). Natural remanent magnetization (NRM) was measured in a magnetically-shielded room at PKU using a 2G-755 cryogenic superconducting quantum interference device (SQUID) rock magnetometer. The Q-ratio, which is the remanent to induced magnetization ratio (Koenigsberger, 1938), was calculated as Q = NRM[A/m]/(Susceptibility[SI] × H[A/m]), where H = 30.24 A/m for the TAG field was obtained from the International Geomagnetic Reference Field (Thébault et al., 2015). Rock samples with $Q > 1$ can retain stable remanent magnetization, while those with $Q < 1$ are dominated by induced magnetization (Koenigsberger, 1938). Anhysteretic remanent magnetization (ARM) was imparted to powder samples packed in gelatin capsules using a D2000 alternating-field (AF) demagnetizer with 120-mT AF, 0.0075 decay rate, and 0.05-mT direct-current bias field. ARM intensity was measured using the 2G-755 magnetometer.

Zhao et al. (1998) reported that sulfides in stockwork samples (Figure S1 and Text S1 in Supporting Information S1) could complicate interpretation of magnetic components when heated above 300–400°C. We therefore conducted AF demagnetization and low-temperature magnetization measurements instead of thermal demagnetization or high-temperature measurements. The NRM was demagnetized by in-line AF coils attached to the 2G-755 magnetometer with 2 mT (0–10 mT), 5 mT (10–50 mT), and 10 mT (50–120 mT) steps. Low-temperature magnetic measurements were performed on powder samples packed in gelatin capsules using a Quantum Design Magnetic Property Measurement System (model MPMS3) at the School of Physics, PKU. Data average time of 5 s was used, which provides a sensitivity of $\sim 10^{-11}$ Am^2 ($\sim 10^{-8}$ emu). Nine selected samples of representative lithology were both zero-field cooled (ZFC) and 2.5-T field-cooled (FC) with a cooling rate of 12 K/min from 300 to 10 K. A low-temperature remanence was imparted after each cooling procedure by a 2.5-T field at 10 K, and then magnetization was tracked in 2 K intervals or continuously when heating the specimen from 10 to 300 K with a 2 K/min rate. Subsequently, a room-temperature remanence was imparted by a 2.5-T field at 300 K, and then magnetization was tracked in 2 K intervals or continuously during low-temperature cycling (LTC) of 300 K – 10 K – 300 K with a 2 K/min rate.

Hysteresis properties were measured using a MicroMag 3900 vibrating sample magnetometer (VSM) at the Institute of Geophysics, China Earthquake Administration in Beijing. For hysteresis loops, a 0.5-T saturation field was used. Hysteresis parameters, including coercivity (B_c), saturation magnetization (M_s), and saturation remanent magnetization (M_{rs}), were obtained after paramagnetic correction using the program HystLab (Paterson

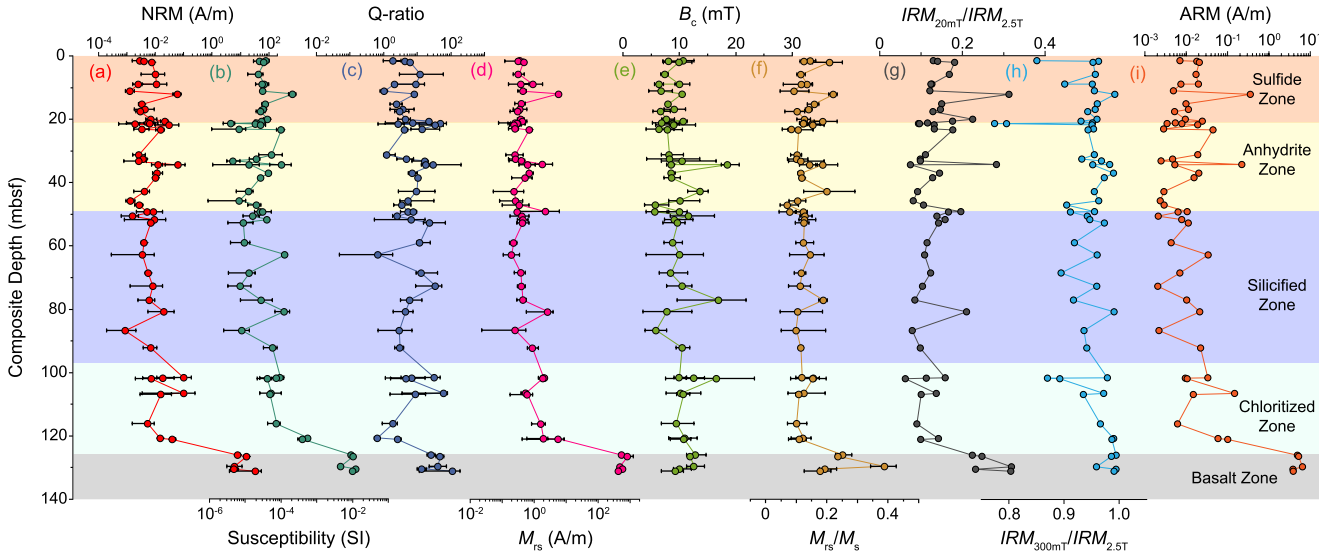

Figure 2. Bulk magnetic parameter variations along the composite columnar section: (a) natural remanent magnetization (NRM), (b) magnetic susceptibility, (c) *Q*-ratio, (d) saturation remanent magnetization (M_{rs}), (e) coercivity (B_c), (f) squareness ratio (saturation remanent magnetization to saturation magnetization ratio, M_{rs}/M_s), (g) contributions of low-coercivity magnetic minerals to the overall isothermal remanent magnetization (IRM) quantified by $IRM_{20mT}/IRM_{2.5T}$, (h) contributions of high-coercivity magnetic minerals to IRM quantified by $IRM_{300mT}/IRM_{2.5T}$, and (i) anhysteretic remanent magnetization (ARM). Data points in (a–f) are averages of three sister specimens with error bars showing the variability of measured three sister specimens. Data points in (g–h) and (i) were obtained from a single IRM or ARM run. Note that all magnetization data are volume-corrected, using volumes calculated from the actual mass of the specimen and the density of the sample. Zonations are as indicated in Figure 1b. The data producing this figure can be found in Data Set S1 of Supporting Information S2.

et al., 2018). First-order reversal curves (FORC; e.g., Roberts et al., 2000) were measured for selected samples of representative lithologies. FORC data were processed using the software FORCinel version 3.06 (Harrison & Feinberg, 2008). Isothermal remanent magnetization (IRM) acquisition curves measured using VSM have noisy data due to weak magnetization of stockwork samples. Therefore, the IRM acquisition curves were remeasured using an ASC Scientific impulse magnetizer and the 2G-755 magnetometer at PKU. A total of 60 data points with a logarithmical distribution from 1 mT to 2.5 T were measured. The IRM data were both unmixed as individual samples using the application MAX Unmix (Maxbauer et al., 2016) based on skewed generalized Gaussian function (Egli, 2003) and as a collection along the composite columnar section using the endmember modeling algorithm of Heslop and Dillon (2007). The IRM acquired at 20 mT, 300 mT, and 2.5 T were extracted to quantify the magnetic contribution from low-coercivity and high-coercivity minerals using ratios of $IRM_{20mT}/IRM_{2.5T}$ and $IRM_{300mT}/IRM_{2.5T}$, respectively.

2.3. Electron Microscopic Analyses

Rock thin sections were prepared for two or three selected samples of each representative lithology. They were carbon-coated and observed using an FEI QUANTA-650 FEG field-emission scanning electron microscope (SEM) at PKU operating at 10–15 kV accelerating voltage and 10 mm working distance. Mineral identification was based on energy-dispersive spectra (EDS).

3. Results

3.1. Bulk Magnetic Parameters

Basalt basement has NRM and susceptibility values of 34.1 A/m and 0.0238 SI (5-sample average), while samples in stockwork (i.e., chloritized, silicified, anhydrite, and sulfide zones) have averaged NRM and susceptibility values of 23.2 mA/m and 1.39×10^{-4} SI (50-sample average; Figure S3 in Supporting Information S1). In stockwork, the chloritized zone samples have NRM and susceptibility values of 65.2 mA/m and 3.40×10^{-4} SI (8-sample average), much higher than others (15.3 mA/m and 0.69×10^{-4} SI; 42-sample average; Figures 2a and 2b and Figures 3a and 3b). The patterns of M_{rs} (Figure 2d) and ARM (Figure 2i) resemble that of NRM and susceptibility, indicating that the low NRM and susceptibility are caused by decreased magnetic mineral

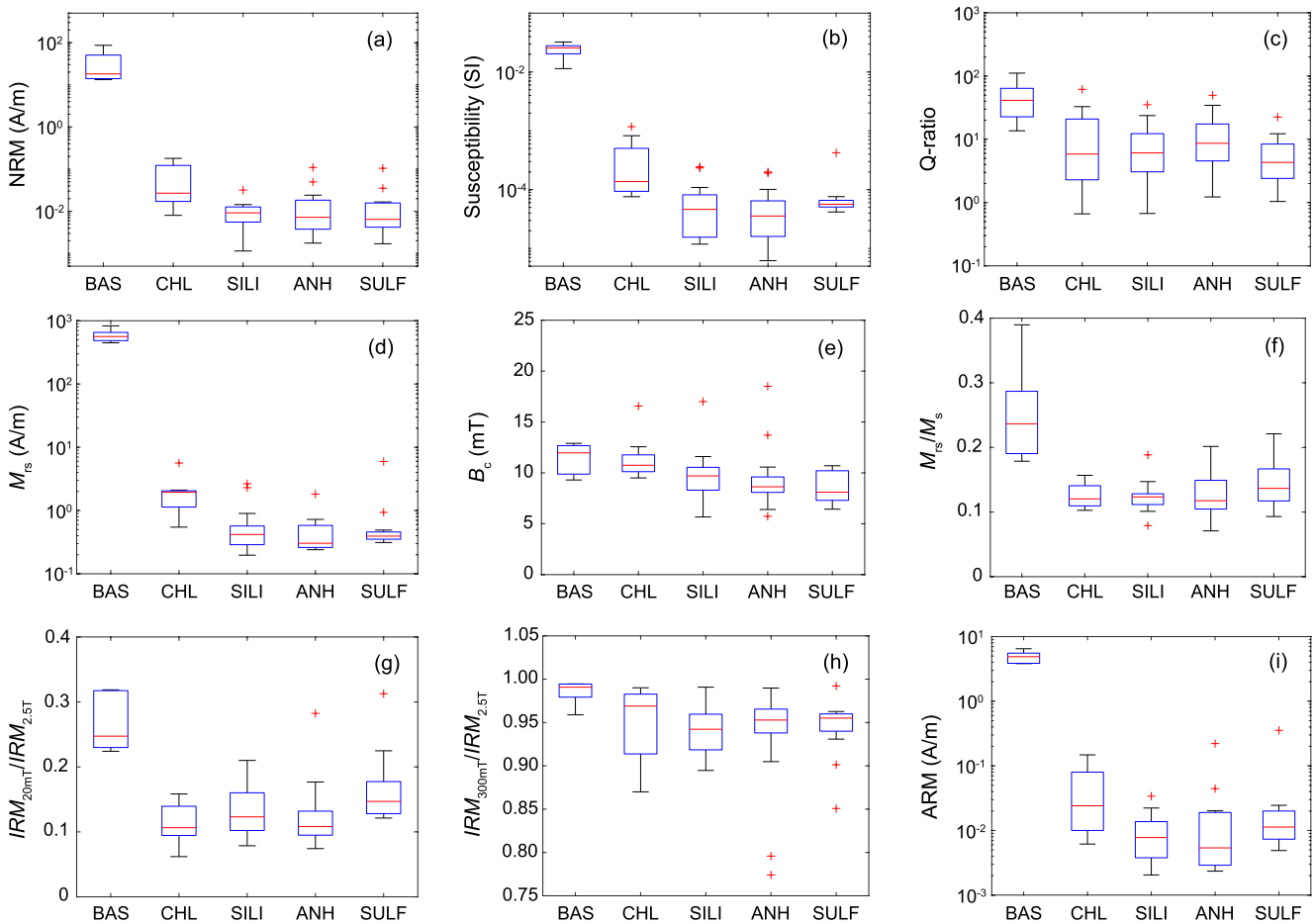

Figure 3. Boxplots of magnetic parameters for samples from different zones. (a–i) correspond to the same parameters shown in Figures 2a–2i. The basalt (BAS), chloritized (CHL), silicified (SILI), anhydrite (ANH), and sulfide (SULF) zones contain 5, 8, 13, 16, and 13 samples. Sample distribution and zonation correspond to those in Figure 1b and Figure S2 of Supporting Information S1. The blue boxes and black segments give 1 and 1.5 interquartile ranges, respectively, while the red lines indicate median values. Red crosses are outliners. The data producing this figure can be found in Data Set S1 of Supporting Information S2.

concentration in stockwork samples. Interestingly, the M_{rs} profile indicates a gradual upward declining trend from silicified to sulfide zones (Figures 2d and 3d); In contrast, ARM (Figures 2i and 3i) shows a gradual upward increasing trend, though it is less evident than $IRM_{20mT}/IRM_{2.5T}$ (Figures 2g and 3g). Similar gradual upward decreasing and increasing trends are observed for B_c (Figures 2e and 3e) and squareness (M_{rs}/M_s; Figures 2f and 3f), respectively. These patterns suggest that fine-grained low-coercivity magnetic minerals are more enriched in the sulfide zone, though the overall concentration of magnetic minerals decreases from chloritized to sulfide zones. Basalt basement samples have $IRM_{300mT}/IRM_{2.5T}$ ratio above 0.95, while most stockwork samples generally have $IRM_{300mT}/IRM_{2.5T}$ around 0.90–0.95 (Figures 2h and 3h), confirming the presence of high-coercivity minerals such as hematite, but their variation pattern is unclear. Spikes in the depth profile (e.g., at ~34–35 mbsf in Figure 2) may be related to isolated chloritized or basaltic clasts in overlying silicified, anhydrite, and sulfide zones transported by hydrothermal fluids (Honnorez et al., 1998; Humphris et al., 1996). It is noteworthy that most samples are more or less inhomogeneous (error bars in Figures 2a–2f).

Fifty three of fifty five samples have Q-ratio above 1 with no noticeable variation trend (Figures 2c and 3c, and Figure S3 in Supporting Information S1), indicating that all lithologies in the stockwork can preserve stable remanent magnetization. The AF demagnetization of NRM reveals that nearly all samples contain strong secondary components that can be easily erased by 20–35 mT AF (Figures 4a–4c). 50 mT AF is sufficient to unblock or demagnetize >90% of the NRM, regardless of sample lithology (Figures 4d–4f). The declination and inclination here are not informative because our studied samples are unoriented. However, these secondary components were also observed in the AF demagnetization results of Zhao et al. (1998) with nearly subvertical inclinations.

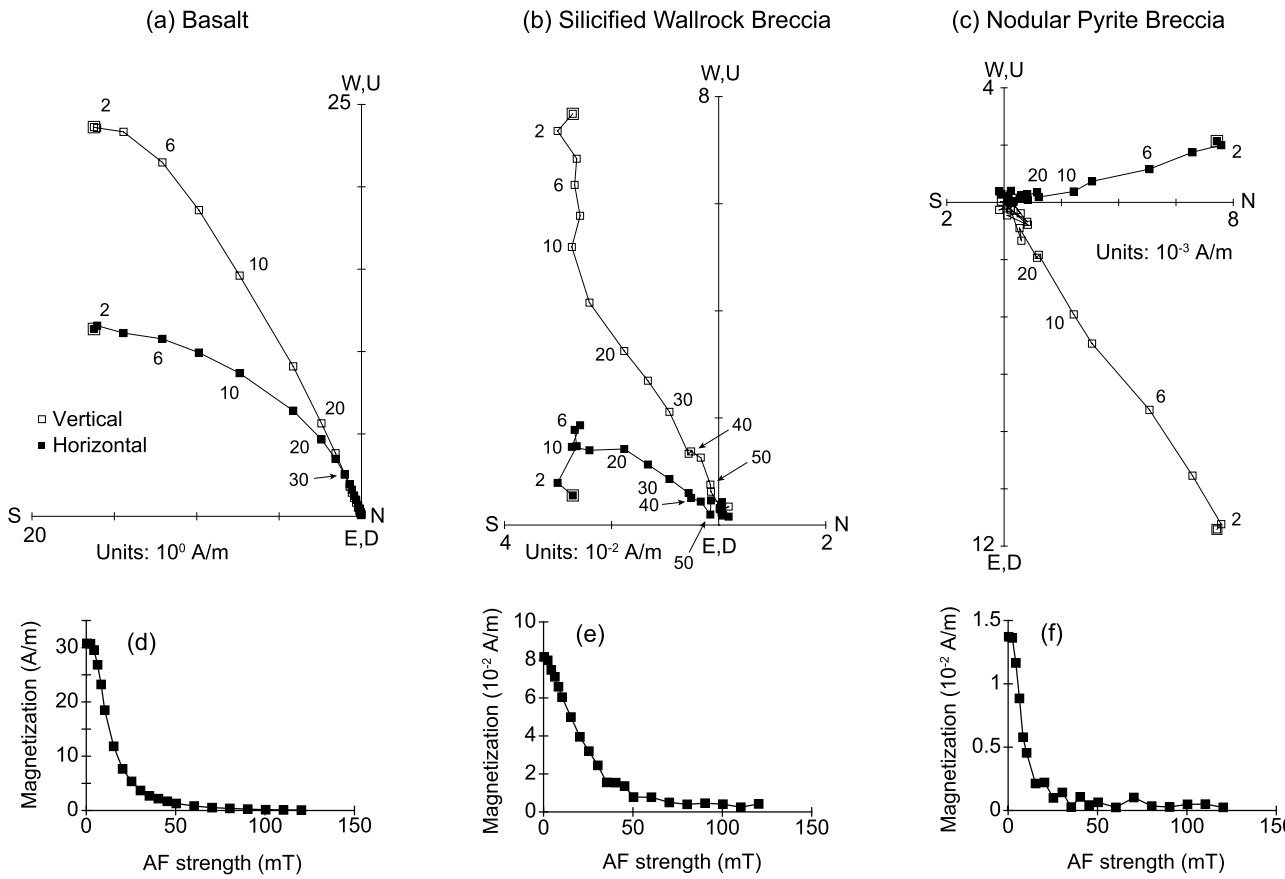

Figure 4. Alternating-field (AF) demagnetization behavior of samples from Trans-Atlantic Geotraverse field. (a–c) Selected representative AF demagnetization plots of (a) basalt (sample 158-957M9R1W90-93), (b) silicified (sample 158-957E12R1W37-40), and (c) sulfide zones (sample 158-957O2R1W14-17). Samples are not unoriented, and the displayed orientation is determined during sample preparation. Double squares indicate natural remanent magnetization. The numbers are labels for typical AF steps with units of millitesla. (d–f) The corresponding variations of magnetization with increasing AF for the samples in (a–c). This plot is made using the software PuffinPlot (Lurcock & Wilson, 2012).

Therefore, analogizing with Zhao et al. (1998), these secondary components are interpreted as drilling-induced remagnetization. In this case, the *Q*-ratio can be deceptive because it overestimates the in situ NRM retained in stockwork samples.

3.2. Unmixed Magnetic Components From IRM Acquisition Curve

Single-sample-based IRM unmixing reveals a three-component regime for all analyzed samples, regardless of their lithologies (Figures 5a–5c). The low-field (blue) components have mean coercivity (B_h) around 20–25 mT (log *B* around 1.3–1.4) and dispersion parameter (*DP*) of 0.25–0.30. The median-field (violet) components have B_h values of 40–65 mT (log *B* around 1.6–1.8) and *DP* values of 0.25–0.30. The high-field (green) components have B_h values above 100 mT (log *B* above 2.0) and *DP* values above 0.35 but are barely saturated under a 2.5-T field. There are abundant low-field (blue) components in the basalt zone (Figure 5a), while the median-field (violet) component becomes dominant for stockwork samples (Figures 5b–5c). Furthermore, the high-field (green) component is more abundant in stockwork samples than in basalt samples.

We use endmember(EM)-based IRM unmixing to verify the observed single-sample-based pattern. We choose three endmembers for calculation based on the coefficient of determination (r^2) (Heslop & Dillon, 2007) and considering the single-sample-based unmixing results. The Four-endmember regime only provides minor improvements in the r^2 value (Figure 5d) and can produce endmembers with significant overlaps in coercivity spectra (Figure S4 in Supporting Information S1). The calculated EM1-EM3 (Figures 5f–5h) resemble the blue, violet, and green components from single-sample unmixing in coercivity spectra (Figures 5a–5c), respectively,

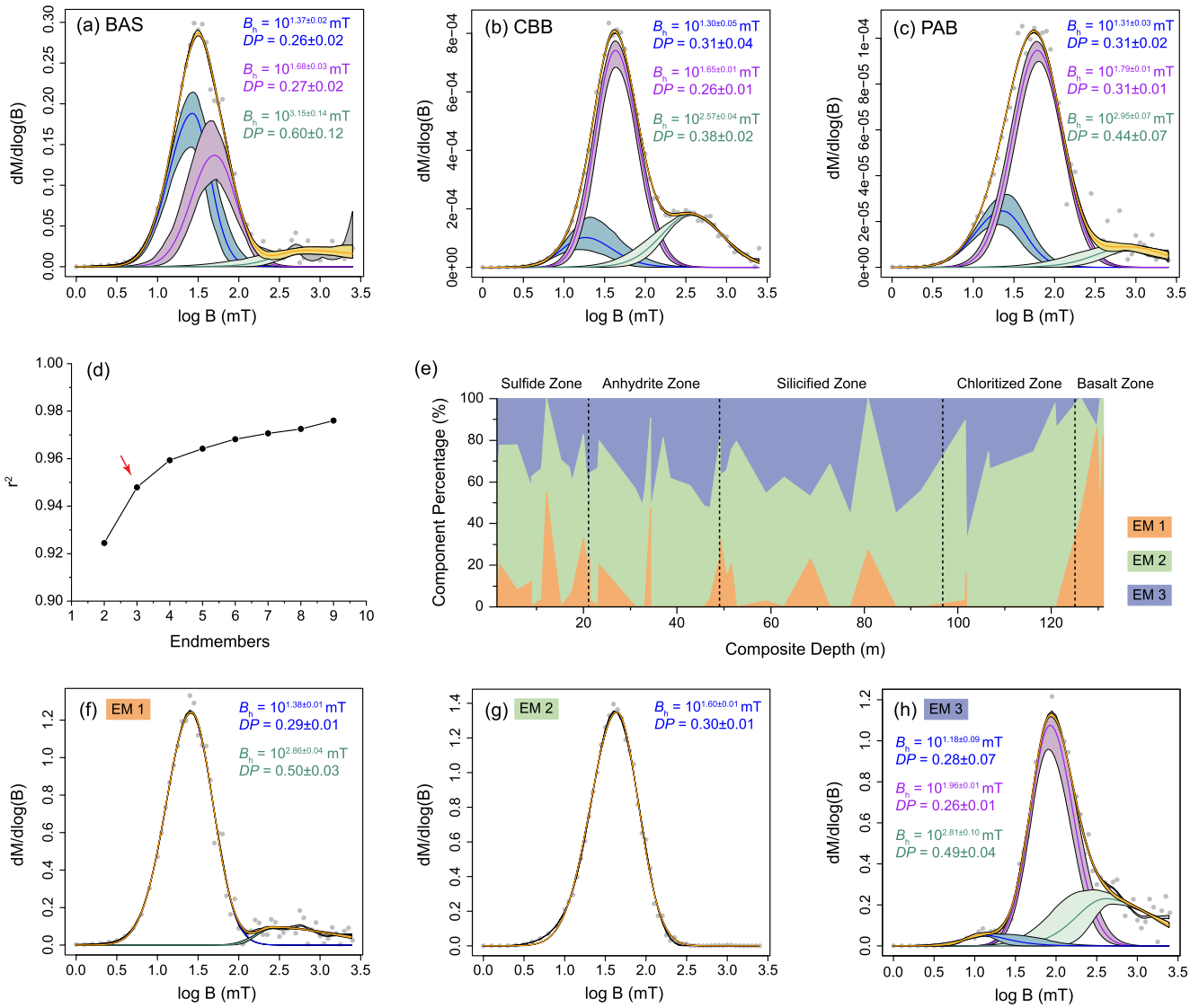

Figure 5. Component unmixing of isothermal remanent magnetization (IRM) acquisition curves. (a–c) Single-sample-based IRM unmixing of representative lithologies: (a) a basalt (BAS) sample (158-957M9R1W90-93), (b) a chloritized basaltic breccia (CBB) sample (158-957E14R1W19-22), and (c) a pyrite-anhydrite breccia (PAB) sample (158-957C7N3W54-56). (d–h) IRM component unmixing based on principal component analysis (PCA). One pyrite-anhydrite breccia sample (158-957G3N1W37-40) is excluded from PCA because of its high data noise. The red arrow in (d) indicates that three endmembers can be an optimal solution. (e) Percentage variation of the three endmembers within the composite columnar section. The zonations are as indicated in Figure 1b. The intrinsic IRM acquisition behavior of each end member is shown in (f–g), respectively.

though there are some overlaps. A similar trend as the single-sample unmixing is observed in the composite columnar section (Figure 5e): EM1 is most abundant in the basalt zone and becomes sporadic in stockwork; EM2 has a trend opposite to that for EM1; EM3 depletes in basalt zone, but gradually increases in chloritized zone and widely occurs in silicified, anhydrite, and sulfide zones.

3.3. Low-Temperature Characterization of Magnetomineralogy

All measured samples show typical magnetite Verwey transition (Verwey, 1939) in LTC and ZFC/FC curves (Figure 6). Verwey transition temperature is 102–104 K for basalt zone and 113–120 K for chloritized, silicified, anhydrite, and sulfide zone samples, indicating magnetite particles in basalt samples are less stoichiometric than those in stockwork samples (Jackson & Moskowitz, 2021). In LTC cooling curves of basalt, chloritized, and silicified zone samples, magnetization gradually decreases towards the Verwey transition, producing a broad shoulder

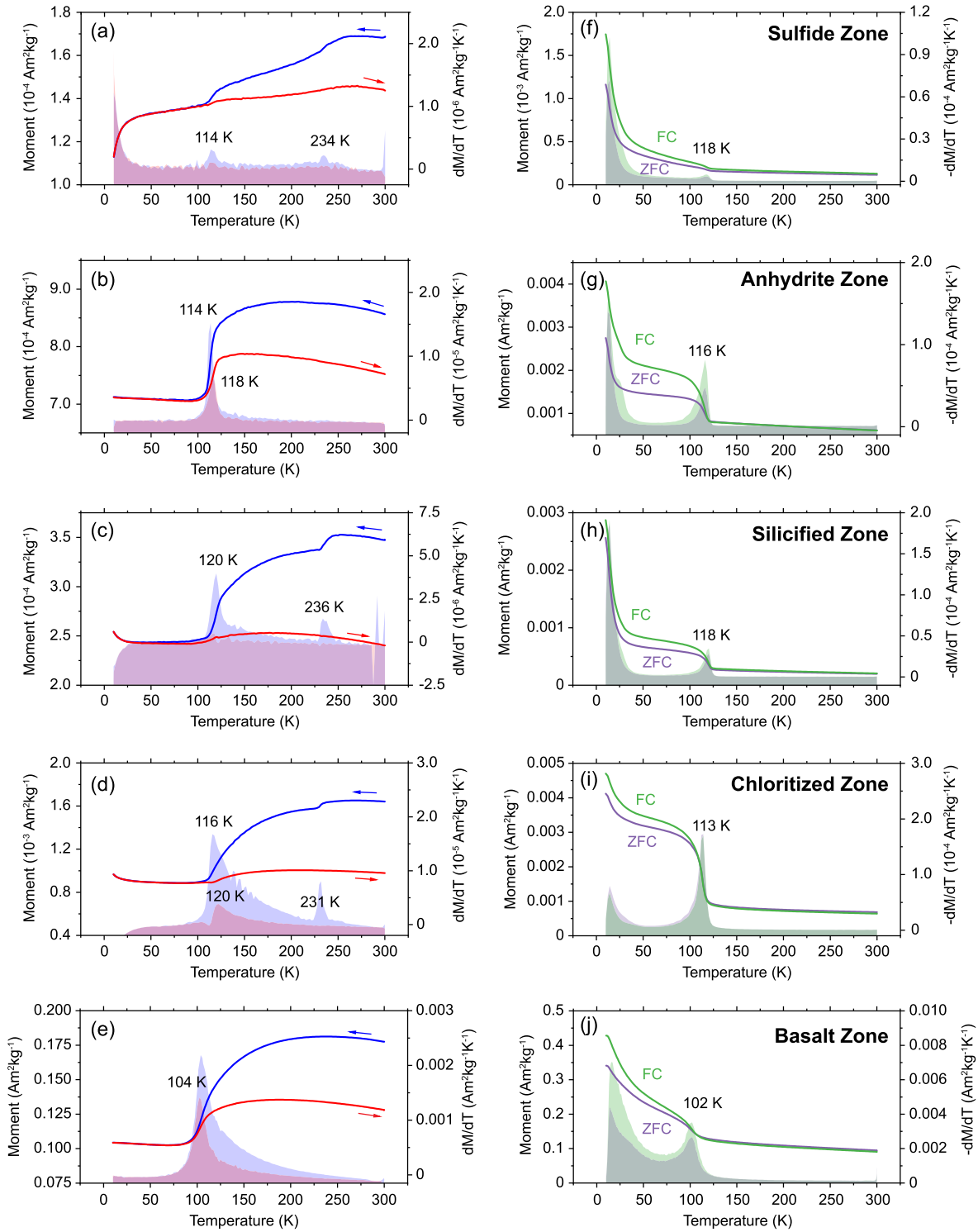

Figure 6. Low-temperature magnetization measurements of representative samples from different zonations as indicated. Panels from bottom to top represent the zonation of the composite columnar section from deep to shallow. (a–e) low-temperature cycling curves of (a) a nodular pyrite breccia sample (158-957H3N1W14-16), (b) a pyrite-silica-anhydrite breccia sample (158-957C11N3W56-58), (c) a silicified wallrock breccia sample (158-957E12R1W37-40), (d) a chloritized basaltic breccia sample (158-957E18R1W33-35), and (e) a basalt sample (158-957M9R1W54-57). Blue and Red arrows indicate cooling and heating curves, respectively. (f–j) Corresponding FC/ZFC curves of (a–e). The plots in the background give the first derivative of each measured low-temperature curve with related colors. Magnetite Verwey transition (Verwey, 1939) and hematite Morin transition (Morin, 1950) are indicated as the peak values in the first derivatives at reported temperature ranges.

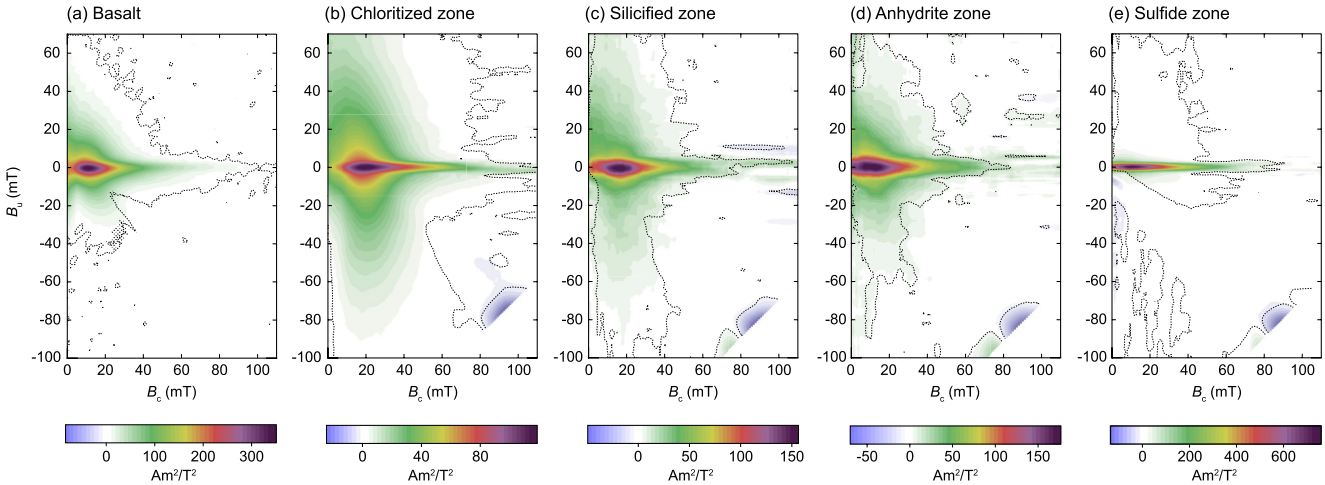

Figure 7. First-order reversal curve (FORC) diagrams of representative samples from different zonations. Panels (a) to (e) are from sample 158-957M9R1W54-57, 158-957E18R1W33-35, 158-957P12R2W37-40, 158-957O4R1W47-49, and 158-957G1N1W11-13, respectively, which represents the zonation of the composite columnar section from bottom to top. Simple smoothing is applied to (a) with a smoothing factor of 4, while the VARIFORC smoothing algorithm (Egli, 2013) is applied to (b–e) with smoothing factors (S_{c0}, S_{c1}, S_{b0}, S_{b1}) of (9, 9, 5, 9), (9, 9, 7, 9), (9, 10, 7, 10), and (7, 8, 4, 8), respectively. Horizontal and vertical lambda values are 0.1 for all samples in (b–e). Dashed lines indicate the 0.05 significance level (Heslop & Roberts, 2012).

above the Verwey transition temperature in first derivatives (Figures 6c–6e). This is due to low-temperature demagnetization (LTD) caused by kinematic domain wall reorganization in multidomain magnetite (Muxworthy & McClelland, 2000). The LTD effect is less evident for anhydrite and sulfide zone samples (Figures 6a and 6b), indicating finer magnetite grains therein. The hematite Morin transition (Morin, 1950) is also recognized in 5 of 9 measured samples (e.g., Figure 6a and Figures 6c and 6d), which corroborates that the high-field IRM components are related to hematite (Figure 5). Endmember-based IRM unmixing results suggest that hematite is likely ubiquitous in all stockwork samples, except for two samples from silicified and sulfide zones (Figure 5e). Samples in Figures 6a–6d and Figures 6f–6i all contain prominent high-field IRM components. Consequently, the absence of hematite Morin transition in some stockwork samples may be due to the overwhelming contribution of magnetite towards the overall magnetization (e.g., Lagroix & Guyodo, 2017). The observed Morin transition temperature range is 230–240 K, indicating that these hematite particles may have submicron sizes (Özdemir et al., 2008). Zhao et al. (1998) suggest that there are small amounts of pyrrhotite in sulfide samples based on a low-temperature transition of around 40 K. But in our analyses, the "40-K transition" has a much lower transition temperature (<25 K) than the Besnus transition at 30–34 K (Rochette et al., 1990). It is evident from ZFC/FC curves that such transitions are likely related to the blocking/unblocking of superparamagnetic or room-temperature paramagnetic mineral phases (Figures 6f–6j).

3.4. Grain Size and Domain State Variations Revealed by FORC Diagrams

In FORC diagrams, basalt samples have vertically dispersed distributions toward the B_u axis ranging approximately −30 to 60 mT and a ridge along $B_u = 0$ axis (Figure 7a), indicating contributions from vortex state and non-interacting single domain (SD) particles (Roberts et al., 2014; Lascu et al., 2018), respectively. Both signals are amplified in chloritized zone samples: vertical dispersion extends to approximately −90 to >70 mT along the B_u axis, and the $B_u = 0$ ridge becomes prominent (Figure 7b). The strongly interacting signals may be related to the intra-particle vortex "superstate" (e.g., Harrison et al., 2002). From chloritized to anhydrite zone samples, the vortex state vertical dispersion has shrunk to the range of about ±60 mT along the B_u axis (Figures 7b–7d). The $B_u = 0$ ridge is comparatively strengthened (Figures 7b–7d). The sulfide zone samples are dominated by non-interacting SD particles with a predominating $B_u = 0$ ridge (Figure 7e). From chloritized to sulfide zones, the coercivity distribution gradually shifts toward the B_u axis (Figures 7b–7e), reconciling with the upward decreasing trend observed for bulk coercivity (Figures 2e and 3e). Overall, the FORC diagrams reveal decreasing grain size for dominating low-coercivity magnetic minerals from chloritized to sulfide zones, consistent with the interpretations of the low-temperature magnetic measurements (Figure 6) and bulk magnetic parameter variations (Figures 2 and 3).

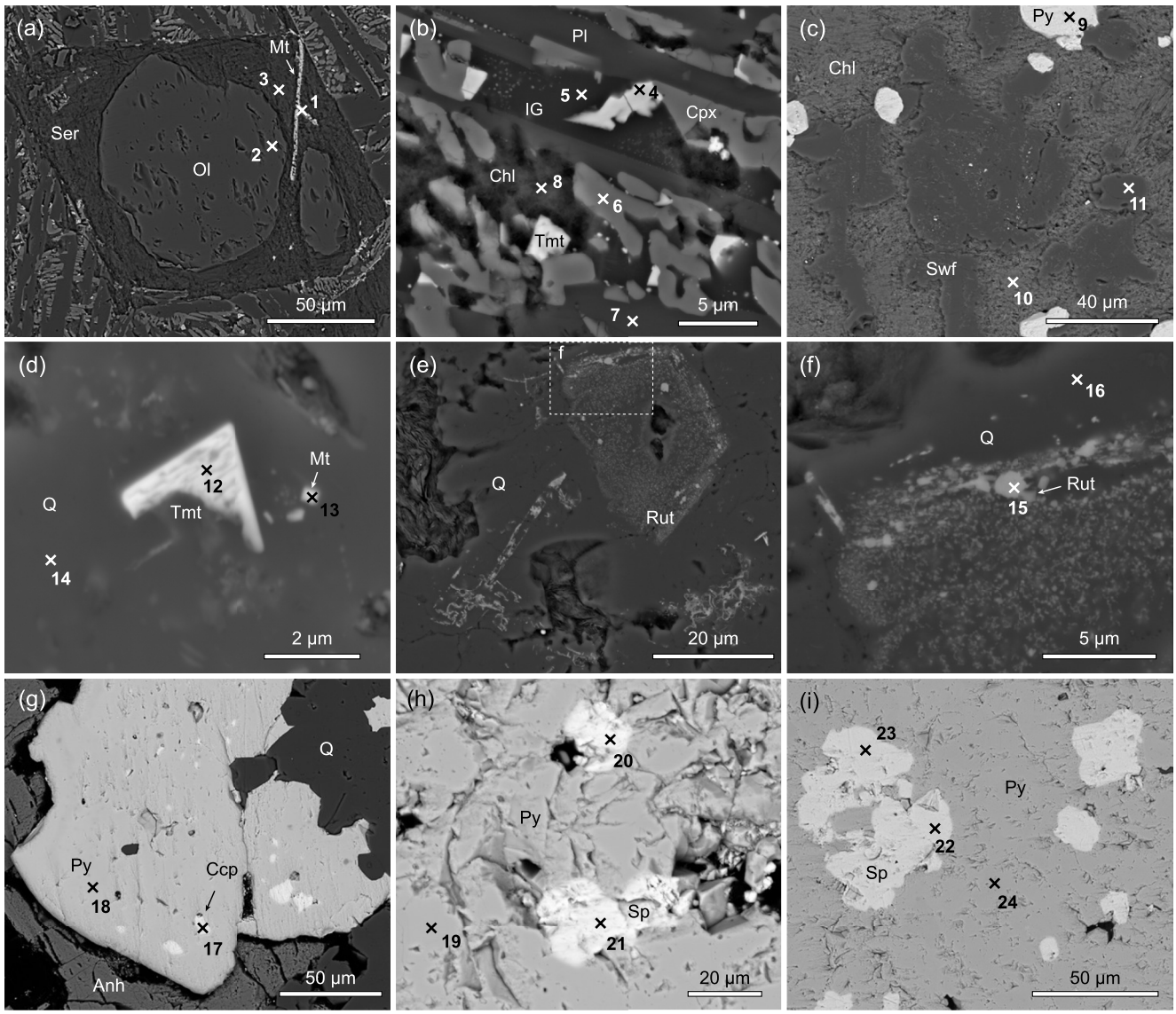

Figure 8. Backscattered electron (BSE) micrographs of magnetic minerals from different lithologies: (a–b) basalt zone sample 158-957M9R1W54-57, (d–c) chloritized zone sample 158-957E18R1W33-35, (e–f) silicified zone sample 158-957P12R2W37-40, (g) anhydrite zone sample 158-957C7N2W33-35, and sulfide zone sample 158-957G1N1W11-13 (h) and 158-957I1N1W28-31 (i). The numbered crosses indicate the energy-dispersive spectra (EDS) spots. Element atomic percentages can be found in Figure S5 and Table S1 in Supporting Information S1. Different mineral phases are as indicated by abbreviations: Anh = anhydrite, Ccp = chalcopyrite, Chl = chlorite, Cpx = clinopyroxene, IG = interstitial glass, Mt = magnetite, Ol = olivine, Pl = plagioclase, Py = pyrite, Q = quartz, Rut = rutile, Ser = serpentine, Sp = sphalerite, Swf = silicified wallrock fragment, Tmt = titanomagnetite.

3.5. Occurrences and Origins of Magnetic Minerals

Basalt zone samples have experienced slight hydrothermal alteration, as evidenced by the serpentinization of olivine phenocrysts (Figure 8a) and the replacement of interstitial glasses by chlorite (Figure 8b). However, the alteration is spatially inhomogeneous: chlorite and interstitial glass coexist on the sides of one plagioclase crystal (Figure 8b). Serpentinization-produced magnetite explains the Verwey transition in low-temperature measurements for the studied basalt zone samples (Figure 6a), while the dominant magnetic minerals in basalt samples are quenching-related titanomagnetite dendrites with Ti substitution (x value) of 0.65 ± 0.06 (averaged for 11 EDS measurements; e.g., spectrum #4 in Figure S5 and Table S1 of Supporting Information S1). Most primary nanoscale titanomagnetite inclusions may have been altered during hydrothermal alteration (e.g., Wang et al., 2020), though some survivors may exist in relatively fresh interstitial glasses (Figure 8b).

The overall magnetic mineral concentration has significantly decreased in chloritized zone samples due to hydrothermal dissolution, similar to the findings of Wang et al. (2020) from the Southwest Indian Ridge Longqi and Yuhuang hydrothermal fields. Some silicified wallrock fragments are found enclosed in chlorite matrix, where two groups of magnetic minerals with different grain sizes, corroborating the interpretations of FORC diagrams (Figure 7b), are embedded in between silicified plagioclase laths (Figures 8c and 8d). The micron-sized group is cratered titanomagnetite with variable titanium content (x values from 0.4 to 0.8; e.g., spectrum #12 in Figure S5 and Table S1 of Supporting Information S1), probably due to their different thermal histories before brecciation (O'Reilly, 1984). The other group is submicron magnetite, and it can be recrystallized from dissolved and exsolved Fe (e.g., Wang et al., 2021). Comparatively, relict Ti produces rutile clusters in silica matrix during enhanced silicification (Figures 8e–8f). Anhydrite and sulfide zone samples contain abundant sulfides. These sulfides are mostly massive pyrite with chalcopyrite and sphalerite inclusions in size of 10–50 μm (Figures 8g–8i). Although FORC diagrams and low-temperature magnetic measurements confirm the existence of fine-grained magnetite and hematite in anhydrite and sulfide zone samples, no ferrimagnetic minerals are directly observed under electron microscopes.

We perform detailed rock magnetic analyses on sulfide sample 158-957I1N1W28-31 to investigate possible sample-scale inhomogeneity of magnetomineralogy (Figures 3a–3f). This sample is chosen because (a) it is an intact corner of a drilled piece and (b) it has relatively strong saturation remanence (5.950 A/m, compared to $\sim 10^{-1}$ A/m of other sulfide samples). The sample was first cut in half using a diamond wire saw and then subsampled using an electric diamond hand mill every 0.2 cm from piece exterior (0 cm) to interior (2 cm) along the central line (Figure 9a). Each subsample was milled into powder with an approximate depth of ~0.5 cm. Hysteresis measurements produce smooth loops (Figure S6 in Supporting Information S1), which show a two-to three-fold decrease in saturation remanence from 0.6 to 1.8 cm, though the outermost 0.6 cm has some scattering (Figure 9b). For crosscheck, the same sample set with 500-mT IRM imparted by VSM was subsequently remeasured using the 2G-755 superconducting magnetometer. Results show a consistent trend with the VSM data (Figure 9b), though magnetic relaxation (in ~48 hr) produced slightly decreased M_{rs} values from the 2G-755 measurements (Table S2 in Supporting Information S1). The coercivity and squareness show no obvious pattern, but FORC diagrams show that the exterior has a more prominent vortex state signal than the interior of the sample (Figures 9c and 9e). It is worth noting that sister specimens for bulk magnetic parameter measurements were cut from the innermost part (~2.0–2.5 cm) and show a dominant non-interacting SD state signal (Figure 7e). The vortex state may explain the scatter of the outmost 0.6 cm in the hysteresis profile (Figure 9b) since contrasting magnetic states are involved during vortex nucleation and annihilation (Lascu et al., 2018). Both near stoichiometric and oxidized magnetite exist in this sample because the identified Verwey transition has a temperature (T_v) of 114–118 K (Figures 9d and 9f) and the LTC curves show a hump between 300 K and T_v (Özdemir & Dunlop, 2010). Together with the decreasing concentration and grain size of magnetic mineral from the piece exterior to the interior, we propose that the sample inhomogeneity may originate from an inward-propagating oxidation gradient (e.g., Fabian & Shcherbakov, 2020).

4. Discussion

The high-temperature hydrothermal alteration model of MORB (Wang et al., 2021) explains most of the magnetic property and magnetomineralogy variations in the TAG basalt, chloritized, and silicified zones. Nevertheless, it is noteworthy that the TAG mound has a slightly different alteration precursor compared to the Southwest Indian Ridge basalts: in addition to micron-scale titanomagnetite dendrites and submicron-scale titanomagnetite inclusions (Figure 8b), the TAG MORB contains olivine phenocrysts which were serpentinized during initial chloritization (Figure 8a), producing magnetite Verwey transition in basalt zone samples (Figures 6e and 6j). The chloritized basaltic breccia samples are petrographically comparable to the fully chloritized samples of Wang et al. (2020, 2021), and therefore a dual Verwey transition pattern is not expected. Nonetheless, cratered titanomagnetite residues in chloritized basaltic breccia samples (Figure 8d) can be evidence for Fe-Ti exsolution (e.g., Wang et al., 2021).

We did not observe in situ ferrimagnetic minerals directly under electron microscopes in anhydrite and sulfide zone samples due to their low concentrations and inconspicuous contrast with pyrite. Magnetic separation has been tried but is also inefficient to extract magnetic remanence carriers because gravitational torque always overrides magnetic torque in the suspension due to the large density of pyrite (~4 g/cm^3, Humphris et al., 1996).

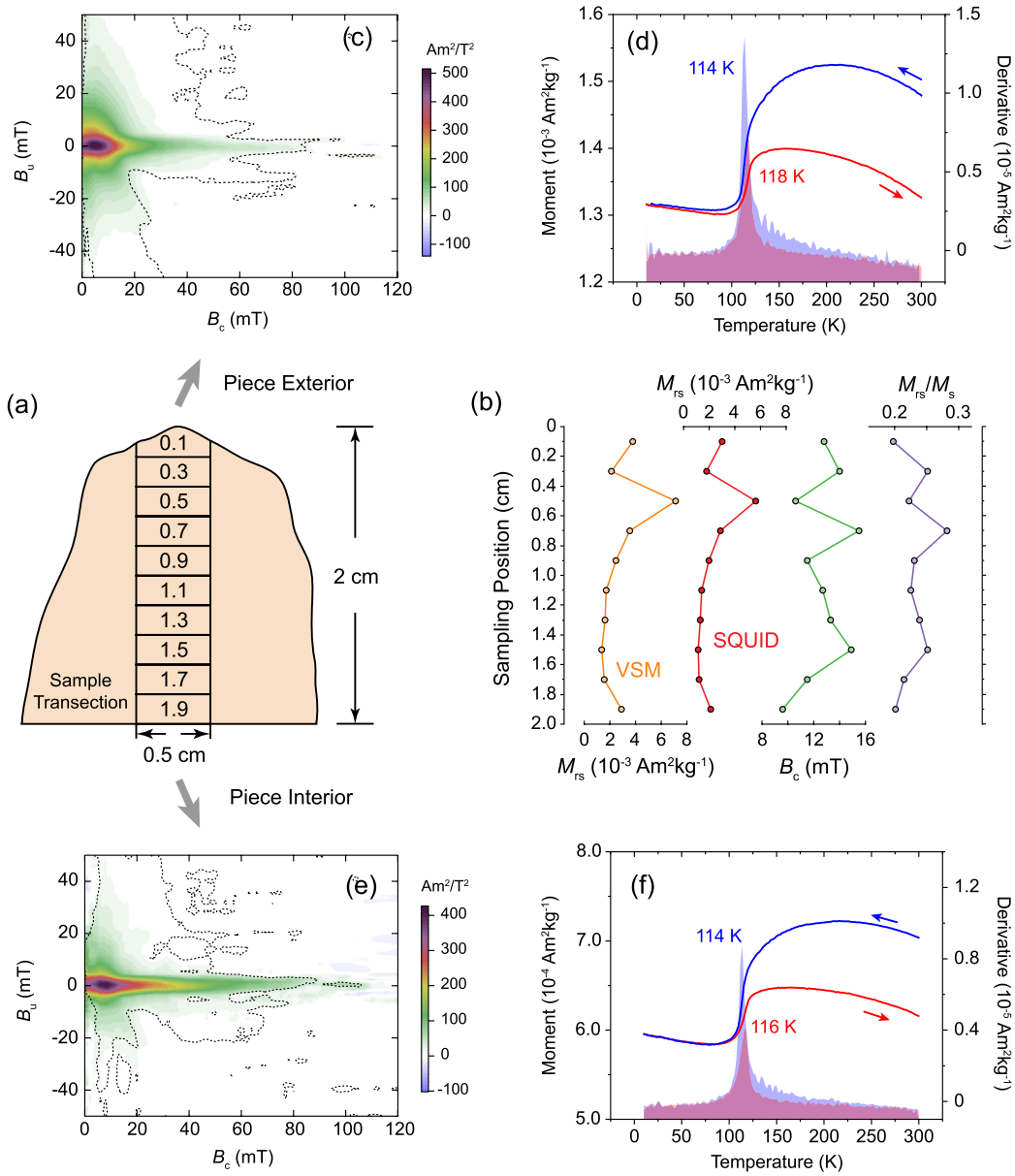

Figure 9. Rock magnetic characterizations of the sample-scale inhomogeneity. (a) A sketch of how subsamples from piece exterior to interior were obtained in a resolution of 0.2 cm. (b) Variations of saturation remanent magnetization (M_{rs}), coercivity (B_c), and squareness (M_{rs}/M_s) from piece exterior to interior. M_{rs} data measured with both a vibrating sample magnetometer (VSM, orange) and a superconducting quantum interference device (SQUID) rock magnetometer (red) are presented, which can be found in Table S2 of Supporting Information S1. Sampling positions are as indicated in (a). The outermost and innermost subsamples have been used to perform first-order reversal curves (FORC) (c and e) and low-temperature measurements (d and f). FORC diagrams were obtained using VARIFORC smoothing (Egli, 2013) with smoothing factors (S_{c0}, S_{c1}, S_{b0}, S_{b1}) of (5, 7, 5, 9) and horizontal and vertical lambda of 0.1. Dashed lines indicate the 0.05 significance level (Heslop & Roberts, 2012). For low-temperature cycling measurements, blue and red curves are cooling and warming curves, as indicated by arrows. The plots in the background indicate the first derivatives, where the magnetite Verwey transition temperature (T_v) is marked respectively for cooling and heating curves.

However, it can be inferred from SEM analyses that magnetic minerals in anhydrite and sulfide zone samples must be related to sulfides, based on the fact that sulfides constitute up to 70%–100% of these samples and hydrothermal alteration has little contribution to the anhydrite and sulfide zone samples (Knott et al., 1998; Figure S1 in Supporting Information S1). Post cruise magnetic analyses by Zhao et al. (1998) have also interpreted that the magnetic minerals in sulfide samples are of chemical origins. Pyrrhotite can be an important magnetic carrier

in sulfides (e.g., Honsho et al., 2016), but this can be excluded here since both petrographic (Knott et al., 1998) and rock magnetic analyses (Figure 6) do not support the ubiquitous presence of pyrrhotite in the TAG mound.

Our sample-scale rock magnetic inhomogeneity test (Figure 9) shows that these sulfide-related magnetic minerals can originate from oxidation. Our rock magnetic analyses reveal similar magnetomineralogy and magnetic properties of sulfide samples to the post-cruise magnetic analyses by Zhao et al. (1998), implying that oxidation during sample storage can be minor. Water is a key oxidation reactant (Fallon et al., 2017) but is kept away from drilled pieces by the constant temperature and humidity in the core repository. Oxidation under seafloor conditions is therefore more likely. It may be related to the drilling process because the decreasing magnetic mineral concentration and grain size from the exterior to the interior of a drilled piece are unlikely to be in situ (Figure 9). Also, drilling-induced secondary remanent magnetization components have been observed during AF demagnetization of NRM (Figure 4; Zhao et al., 1998). One of the major aftermaths of drilling is the entrainment of seawater into the stockwork (Humphris et al., 1996). At temperatures between ~150 and 300°C (considering the presence of anhydrite and its role in hydrothermal mineralization; Guo et al., 2020), the addition of sulfate from seawater will oxidize Fe^{2+} to Fe^{3+} (Shen & Buick, 2004):

$$8Fe^{2+} + 10H^{+} + SO_4^{2-} \rightarrow 8Fe^{3+} + H_2S + 4H_2O \quad (1)$$

At the same time, Fe^{2+} and Fe^{3+} can form magnetite through the following series of reactions (Iwasaki et al., 2012):

$$Fe^{2+} + 2OH^{-} \rightarrow Fe(OH)_2 \quad (2)$$

$$Fe^{3+} + 3OH^{-} \rightarrow Fe(OH)_3 \quad (3)$$

$$Fe(OH)_3 \rightarrow \alpha FeOOH + H_2O \quad (4)$$

$$Fe(OH)_2 + 2\alpha FeOOH \rightarrow Fe_3O_4 + 2H_2O \quad (5)$$

Pre-drilling oxidation may also be involved since almost all samples in the stockwork have high-coercivity hematite components (Figure 5e), which can form under ambient seafloor conditions (Fallon et al., 2017):

$$2FeS_2 + 7.5O_2(aq) + 4H_2O \rightarrow Fe_2O_3 + 4SO_4^{2-} + 8H^{+} \quad (6)$$

Seafloor oxidation prior to drilling is also supported by the presence of red chert in other ODP Leg 158 holes (Humphris et al., 1996) and the fact that oxidative seawater can circulate to tens of meters beneath the TAG active mound (Pontbriand & Sohn, 2014; Tivey et al., 1995). It should be pointed out that little is known regarding the reaction rate of the aforementioned two oxidation paths (Fallon et al., 2017), but both pathways can certainly modify the magnetic properties of SMS deposits.

Our findings suggest that the physicochemical properties of SMS deposits are susceptible to disturbance from external environments. Drilling-induced oxidation can be a major concern because it releases heavy metal contents (Meng et al., 2021; Hu et al., 2022), which may have potential environmental impacts on hydrothermal ecosystems (Van Dover, 2019; Orcutt et al., 2020). On the other hand, attention should be paid to the potentially widespread seafloor oxidation during geological preservations of SMS deposits. From the perspective of magnetic properties, although oxidation produces subtle variations in bulk rock magnetic parameters in the TAG active mound (Figures 2 and 3), it can play an essential role in inactive and extinct mounds with longstanding exposure to oxidative seafloor environments. Neoformation of magnetite and hematite may complement the decreased magnetization in seafloor hydrothermal fields, complicating the interpretations of magnetic surveying data. For example, sulfides from inactive mounds of Longqi and Yuhuang hydrothermal fields in the Southwest Indian Ridge have enhanced NRM compared to fully chloritized basaltic breccia samples, partly due to oxidation-produced magnetite and hematite (Wang et al., 2020). In the TAG inactive mounds, gossan has been found as the caprock of SMS deposits (Murton et al., 2019). Although its magnetic property has not been systematically studied, there are cases where these iron-oxides and iron-oxyhydroxides contribute to the vent field magnetic anomalies (e.g., Gee et al., 2001).

Despite its significance, our knowledge of the potential oxidation of SMS deposits is still limited. One of the overlooked factors is the galvanic reactions between different polymetallic sulfides, as they have different rest potentials and seawater can serve as the required electrolyte (Fallon et al., 2017). Migrating electrons produce current

in SMS deposits, creating spontaneous "geobattery" (Sato & Mooney, 1960). Seafloor self-potential surveys have shown that SMS deposits in inactive hydrothermal mounds have strong electric anomalies (Szitkar et al., 2021; Zhu et al., 2020) and therefore confirm the existence of galvanic reactions in SMS deposits. Laboratory simulations have verified that galvanic reactions can accelerate the oxidation rates of sulfides (Knight et al., 2018). Although applying such observations to seafloor conditions remains challenging, these findings call for attention to the galvanic reactions. Overall, the galvanic reaction is only one of those controlling factors. More efforts, including but not limited to combined laboratory simulations and field observations, are needed to delineate how others affect the oxidation of SMS deposits. As SMS deposits are considered potential targets for mining (Szitkar et al., 2021; Van Dover, 2019), such knowledge is instructive for understanding the complicated physicochemical properties of SMS deposits, which may ultimately contribute to designing future exploitation strategies.

5. Conclusions

A composite stratigraphic columnar section covering the basaltic basement and stockwork of the TAG active mound was constructed from multiple ODP Leg 158 drill holes. Bulk magnetic parameter measurements reveal an overall low magnetic mineral concentration in the stockwork. Comprehensive rock magnetic and electron microscopic analyses reveal that the hydrothermal alteration model of Wang et al. (2020, 2021) explains the occurrence of titanomagnetite and magnetite in chloritized and silicified zone samples. Although no ferrimagnetic minerals are directly observed using an electron microscope in anhydrite and sulfide zone samples, we provide rock magnetic evidence that they contain magnetite and hematite originated from oxidation of sulfides during drilling or under ambient seafloor conditions. Our results disclose that the magnetic properties of SMS deposits are sensitive to seafloor oxidative environments. Oxidation-related magnetite and hematite can potentially serve as magnetic fingerprints for distinguishing polymetallic sulfides from other hydrothermal products using magnetic surveying methods, which is essential for probing the complex structures beneath seafloor hydrothermal fields and prospection of SMS deposits. However, on the other hand, we recognize that our current knowledge remains insufficient in diagnosing the physicochemical mechanism of polymetallic sulfide oxidation both under ambient seafloor environments and during drilling or mining activities. These findings arouse the necessity of multi-disciplinary studies on the physicochemical alteration of SMS deposits before designing future exploration and exploitation strategies for SMS deposits.

Data Availability Statement

All rock magnetic data in this study are available at Peking University Open Research Data Platform (https://doi.org/10.18170/DVN/VXHZSP). Text S2 in Supporting Information S1 describes the data structure and instructs on usage.

References

Caratori Tontini, F., Crone, T. J., deRonde, C. E. J., Fornari, D. J., Kinsey, J. C., Mittelstaedt, E., & Tivey, M. (2016). Crustal magnetization and the subseafloor structure of the ASHES vent field, Axial Seamount, Juan de Fuca Ridge: Implications for the investigation of hydrothermal sites. *Geophysical Research Letters*, *43*(12), 6205–6211. https://doi.org/10.1002/2016GL069430

Egli, R. (2003). Analysis of the field dependence of remanent magnetization curves. *Journal of Geophysical Research*, *108*(B2), 2081. https://doi.org/10.1029/2002JB002023

Egli, R. (2013). VARIFORC: An optimized protocol for calculating non-regular first-order reversal curve (FORC) diagrams. *Global and Planetary Change*, *110*, 302–320. https://doi.org/10.1016/j.gloplacha.2013.08.003

Fabian, K., & Shcherbakov, V. P. (2020). The magnetization of the ocean floor: Stress and fracturing of titanomagnetite particles by low-temperature oxidation. *Geophysical Journal International*, *221*(3), 2104–2112. https://doi.org/10.1093/gji/ggaa142

Fallon, E. K., Petersen, S., Brooker, R. A., & Scott, T. B. (2017). Oxidative dissolution of hydrothermal mixed-sulphide ore: An assessment of current knowledge in relation to seafloor massive sulphide mining. *Ore Geology Reviews*, *86*, 309–327. https://doi.org/10.1016/j.oregeorev.2017.02.028

Galley, C., Lelièvre, P., Haroon, A., Graber, S., Jamieson, J., Szitkar, F., et al. (2021). Magnetic and gravity surface geometry inverse modeling of the TAG active mound. *Journal of Geophysical Research: Solid Earth*, *126*(10), e2021JB022228. https://doi.org/10.1029/2021JB022228

Gee, J. S., Webb, S. C., Ridgway, J., Staudigel, H., & Zumberge, M. A. (2001). A deep tow magnetic survey of Middle Valley, Juan de Fuca Ridge. *Geochemistry, Geophysics, Geosystems*, *2*(11), 2001GC000170. https://doi.org/10.1029/2001GC000170

Gehrmann, R. A. S., North, L. J., Graber, S., Szitkar, F., Petersen, S., Minshull, T. A., & Murton, B. J. (2019). Marine mineral exploration with controlled source electromagnetics at the TAG hydrothermal field, 26°N, Mid-Atlantic Ridge. *Geophysical Research Letters*, *46*(11), 5808–5816. https://doi.org/10.1029/2019GL082928

German, C. R., & Seyfried, W. E., Jr. (2014). Hydrothermal processes. *Treatise on Geochemistry*, *8*, 191–233. (2nd ed.). https://doi.org/10.1016/B978-0-08-095975-7.00607-0

Acknowledgments

This research used samples provided by the International Ocean Discovery Program (IODP). This study was supported by a Royal Society-Newton Advanced Fellowship (RS-NAF) to L.C. The RS-NAF is jointly funded by the National Natural Science Foundation of China (NSFC grant 42061130214) and the RS (grant NAF\R1\201096). We thank additional support from the COMRA Major Project under contract No. DY135-S1-01-06. The manuscript has benefited from comments and suggestions from two anonymous reviewers. Efficient editorial handling by editor Joshua Feinberg is greatly appreciated.

Guo, Z., Rüpke, L. H., Fuchs, S., Iyer, K., Hannington, M. D., Chen, C., et al. (2020). Anhydrite-assisted hydrothermal metal transport to the ocean floor—Insights from thermo-hydro-chemical modeling. *Journal of Geophysical Research: Solid Earth*, *125*(7), e2019JB019035. https://doi.org/10.1029/2019JB019035

Hannington, M., Jamieson, J., Monecke, T., Petersen, S., & Beaulieu, S. (2011). The abundance of seafloor massive sulfide deposits. *Geology*, *39*(12), 1155–1158. https://doi.org/10.1130/G32468.1

Harrison, R. J., Dunin-Borkowski, R. E., & Putnis, A. (2002). Direct imaging of nanoscale magnetic interactions in minerals. *Proceedings of the National Academy of Sciences of the United States of America*, *99*(26), 16556–16561. https://doi.org/10.1073/pnas.262514499

Harrison, R. J., & Feinberg, J. M. (2008). FORCinel: An improved algorithm for calculating first-order reversal curve distributions using locally weighted regression smoothing. *Geochemistry, Geophysics, Geosystems*, *9*(5), Q05016. https://doi.org/10.1029/2008GC001987

Heslop, D., & Dillon, M. (2007). Unmixing magnetic remanence curves without a priori knowledge. *Geophysical Journal International*, *170*(2), 556–566. https://doi.org/10.1111/j.1365-246X.2007.03432.x

Heslop, D., & Roberts, A. P. (2012). Estimation of significance levels and confidence intervals for first-order reversal curve distributions. *Geochemistry, Geophysics, Geosystems*, *13*, Q12Z40. https://doi.org/10.1029/2012GC004115

Honnorez, J. J., Alt, J. C., & Humphris, S. E. (1998). Vivisection and autopsy of active and fossil hydrothermal alterations of basalt beneath and within the TAG hydrothermal mound. In P. M.Herzig, S. E.Humphris, D. J.Miller, & R. A.Zierenberg (Eds.), *Proceedings of the ocean drilling program, scientific results* (Vol. 158, pp. 231–254). https://doi.org/10.2973/odp.proc.sr.158.219.1998

Honsho, C., Yamazaki, T., Ura, T., Okino, K., Morozumi, H., & Ueda, S. (2016). Magnetic anomalies associated with abundant production of pyrrhotite in a sulfide deposit in the Okinawa Trough, Japan. *Geochemistry, Geophysics, Geosystems*, *17*, 4413–4424. https://doi.org/10.1002/2016GC006480

Hu, S., Tao, C., Liao, S., Zhu, C., & Qiu, Z. (2022). Transformation of minerals and mobility of heavy metals during oxidation weathering of seafloor massive sulfide and their environmental significance. *The Science of the Total Environment*, *819*, 153091. https://doi.org/10.1016/j.scitotenv.2022.153091

Humphris, S. E., Herzig, P. M., & Miller, D. J., & Shipboard Scientific Party. (1996). *Proceedings of the ocean drilling program*. Ocean Drilling Program. Initial Reports, 158. https://doi.org/10.2973/odp.proc.ir.158.1996

Humphris, S. E., Herzig, P. M., Miller, D. J., Alt, J. C., Becker, K., Brown, D., et al. (1995). The internal structure of an active sea-floor massive sulphide deposit. *Nature*, *377*(6551), 713–716. https://doi.org/10.1038/377713a0

Humphris, S. E., Tivey, M. K., & Tivey, M. A. (2015). The Trans-Atlantic Geotraverse hydrothermal field: A hydrothermal system on an active detachment fault. *Deep-Sea Research II*, *121*, 8–16. https://doi.org/10.1016/j.dsr2.2015.02.015

Iwasaki, T., Mizutani, N., Watano, S., Yanagida, T., & Kawai, T. (2012). Hydrothermal synthesis of magnetite nanoparticles via sequential formation of iron hydroxide precipitates. *Journal of Experimental Nanoscience*, *7*(4), 355–365. https://doi.org/10.1080/17458080.2010.515250

Jackson, M. J., & Moskowitz, B. (2021). On the distribution of Verwey transition temperatures in natural magnetites. *Geophysical Journal International*, *224*(2), 1314–1325. https://doi.org/10.1093/gji/ggaa516

Knight, R. D., Roberts, S., & Cooper, M. J. (2018). Investigating monomineralic and polymineralic reactions during the oxidation of sulphide minerals in seawater: Implications for mining seafloor massive sulphide deposits. *Applied Geochemistry*, *90*, 63–74. https://doi.org/10.1016/j.apgeochem.2017.12.027

Knott, R., Fouquet, Y., Honnorez, J., Petersen, S., & Bohn, M. (1998). Petrology of hydrothermal mineralization: A vertical section through the TAG mound. In P. M.Herzig, S. E.Humphris, D. J.Miller, & R. A.Zierenberg (Eds.), *Proceedings of the ocean drilling program, scientific results* (Vol. 158, pp. 5–26). https://doi.org/10.2973/odp.proc.sr.158.201.1998

Koenigsberger, J. G. (1938). Natural residual magnetism of eruptive rocks. *Terrestrial Magnetism and Atmospheric Electricity*, *43*(2), 119–130. https://doi.org/10.1029/TE043i002p00119

Lagroix, F., & Guyodo, Y. (2017). A new tool for separating the magnetic mineralogy of complex mineral assemblages from low temperature magnetic behavior. *Frontiers of Earth Science*, *5*, 61. https://doi.org/10.3389/feart.2017.00061

Lascu, I., Einsle, J. F., Ball, M. R., & Harrison, R. J. (2018). The vortex state in geologic materials: A micromagnetic perspective. *Journal of Geophysical Research: Solid Earth*, *123*(9), 7285–7304. https://doi.org/10.1029/2018JB015909

Lurcock, P. C., & Wilson, G. S. (2012). PuffinPlot: A versatile, user-friendly program for paleomagnetic analysis. *Geochemistry, Geophysics, Geosystems*, *13*(6), Q06Z45. https://doi.org/10.1029/2012GC004098

Maxbauer, D. P., Feinberg, J. M., & Fox, D. L. (2016). MAX Unmix: A web application for unmixing magnetic coercivity distributions. *Computers & Geosciences*, *95*, 140–145. https://doi.org/10.1016/j.cageo.2016.07.009

Meng, X., Jin, X., Li, X., Chu, F., Zhang, W., Wang, H., et al. (2021). Mineralogy and geochemistry of secondary minerals and oxyhydroxides from the Xunmei hydrothermal field, Southern Mid-Atlantic Ridge (26°S): Insights for metal mobilization during the oxidation of submarine sulfides. *Marine Geology*, *442*, 106654. https://doi.org/10.1016/j.margeo.2021.106654

Morin, F. J. (1950). Magnetic susceptibility of αFe_2O_3 and αFe_2O_3 with added titanium. *Physical Review*, *78*(6), 819–820. https://doi.org/10.1103/PhysRev.78.819.2

Murton, B. J., Lehrmann, B., Dutrieux, A. M., Martins, S., dela Iglesia, A. G., Stobbs, I. J., et al. (2019). Geological fate of seafloor massive sulphides at the TAG hydrothermal field (Mid-Atlantic Ridge). *Ore Geology Reviews*, *107*, 903–925. https://doi.org/10.1016/j.oregeorev.2019.03.005

Muxworthy, A. R., & McClelland, E. (2000). The causes of low-temperature demagnetization of remanence in multidomain magnetite. *Geophysical Journal International*, *140*(1), 115–131. https://doi.org/10.1046/j.1365-246x.2000.00000.x

Orcutt, B. N., Bradley, J. A., Brazelton, W. J., Estes, E. R., Goordial, J. M., Huber, J. A., et al. (2020). Impacts of deep-sea mining on microbial ecosystem services. *Limnology & Oceanography*, *65*(7), 1489–1510. https://doi.org/10.1002/lno.11403

O'Reilly, W. (1984). *Rock and mineral magnetism*. Blackie & Son. Ltd.

Özdemir, Ö., & Dunlop, D. J. (2010). Hallmarks of maghemitization in low-temperature remanence cycling of partially oxidized magnetite nanoparticles. *Journal of Geophysical Research*, *115*(B2), B02101. https://doi.org/10.1029/2009JB006756

Özdemir, Ö., Dunlop, D. J., & Berquó, T. S. (2008). Morin transition in hematite: Size dependence and thermal hysteresis. *Geochemistry, Geophysics, Geosystems*, *9*(10), Q10Z01. https://doi.org/10.1029/2008GC002110

Paterson, G. A., Zhao, X., Jackson, M., & Heslop, D. (2018). Measuring, processing, and analyzing hysteresis data. *Geochemistry, Geophysics, Geosystems*, *19*(7), 1925–1945. https://doi.org/10.1029/2018GC007620

Pontbriand, C. W., & Sohn, R. A. (2014). Microearthquake evidence for reaction-driven cracking within the Trans-Atlantic Geotraverse active hydrothermal deposit. *Journal of Geophysical Research: Solid Earth*, *119*(2), 822–839. https://doi.org/10.1002/2013JB010110

Roberts, A. P., Heslop, D., Zhao, X., & Pike, C. R. (2014). Understanding fine magnetic particle systems through use of first-order reversal curve diagrams. *Reviews of Geophysics*, *52*(4), 557–602. https://doi.org/10.1002/2014RG000462

Roberts, A. P., Pike, C. R., & Verosub, K. L. (2000). First-order reversal curve diagrams: A new tool for characterizing the magnetic properties of natural samples. *Journal of Geophysical Research*, *105*(B12), 28461–28475. https://doi.org/10.1029/2000JB900326

Rochette, P., Fillion, G., Mattéi, J.-L., & Dekkers, M. J. (1990). Magnetic transition at 30–34 Kelvin in pyrrhotite: Insight into a widespread occurrence of this mineral in rocks. *Earth and Planetary Science Letters*, *98*(3–4), 319–328. https://doi.org/10.1016/0012-821X(90)90034-U

Roman, C., & Singh, H. (2007). A self-consistent bathymetric mapping algorithm. *Journal of Field Robotics*, *24*(1–2), 23–50. https://doi.org/10.1002/rob.20164

Rona, P. A., Klinkhammer, G., Nelsen, T. A., Trefry, J. H., & Elderfield, H. (1986). Black smokers, massive sulphides and vent biota at the Mid-Atlantic Ridge. *Nature*, *321*(6065), 33–37. https://doi.org/10.1038/321033a0

Sato, M., & Mooney, H. M. (1960). The electrochemical mechanism of sulfide self-potentials. *Geophysics*, *25*(1), 226–249. https://doi.org/10.1190/1.1438689

Schwarzenbach, E. M., & Steele-MacInnis, M. (2020). Fluids in submarine mid-ocean ridge hydrothermal settings. *Elements*, *16*(6), 389–394. https://doi.org/10.2138/gselements.16.6.389

Shen, Y., & Buick, R. (2004). The antiquity of microbial sulfate reduction. *Earth-Science Reviews*, *64*(3–4), 243–272. https://doi.org/10.1016/S0012-8252(03)00054-0

Szitkar, F., Dyment, J., Choi, Y., & Fouquet, Y. (2014). What causes low magnetization at basalt-hosted hydrothermal sites? Insights from inactive site Krasnov (MAR 16°38' N). *Geochemistry, Geophysics, Geosystems*, *15*(4), 1441–1451. https://doi.org/10.1002/2014GC005284

Szitkar, F., Hölz, S., Tarits, P., & Petersen, S. (2021). Deep-sea electric and magnetic surveys over active and inactive basalt-hosted hydrothermal sites of the TAG segment (26°, MAR): An optimal combination for seafloor massive sulfide exploration. *Journal of Geophysical Research: Solid Earth*, *126*(10), e2021JB022082. https://doi.org/10.1029/2021JB022082

Thébault, E., Finlay, C. C., Beggan, C. D., Alken, P., Aubert, J., Barrois, O., et al. (2015). International Geomagnetic Reference Field: The 12th generation. *Earth Planets and Space*, *67*(1), 79. https://doi.org/10.1186/s40623-015-0228-9

Tivey, M. A., & Johnson, H. P. (2002). Crustal magnetization reveals subsurface structure of Juan de Fuca Ridge hydrothermal vent fields. *Geology*, *30*(11), 979–982. https://doi.org/10.1130/0091-7613(2002)030<0979:CMRSSO>2.0.CO;2

Tivey, M. A., Rona, P. A., & Schouten, H. (1993). Reduced crustal magnetization beneath the active sulfide mound, TAG hydrothermal field, Mid-Atlantic Ridge at 26°N. *Earth and Planetary Science Letters*, *115*(1–4), 101–115. https://doi.org/10.1016/0012-821X(93)90216-V

Tivey, M. K. (2007). Generation of seafloor hydrothermal vent fluids and associated mineral deposits. *Oceanography*, *20*(1), 50–65. https://doi.org/10.5670/oceanog.2007.80

Tivey, M. K., Humphris, S. E., Thompson, G., Hannington, M. D., & Rona, P. A. (1995). Deducing patterns of fluid flow and mixing within the TAG active hydrothermal mound using mineralogical and geochemical data. *Journal of Geophysical Research*, *100*(7), 12527–12555. https://doi.org/10.1029/95JB00610

Van Dover, C. L. (2019). Inactive sulfide ecosystems in the deep sea: A review. *Frontiers in Marine Science*, *6*, 461. https://doi.org/10.3389/fmars.2019.00461

Verwey, E. J. W. (1939). Electronic conduction of magnetite (Fe_3O_4) and its transition point at low temperatures. *Nature*, *144*(3642), 327–328. https://doi.org/10.1038/144327b0

Wang, S., Chang, L., Tao, C., Bilardello, D., Liu, L., & Wu, T. (2021). Seafloor magnetism under hydrothermal alteration: Insights from magnetomineralogy and magnetic properties of the Southwest Indian Ridge Basalts. *Journal of Geophysical Research: Solid Earth*, *126*(12), e2021JB022646. https://doi.org/10.1029/2021JB022646

Wang, S., Chang, L., Wu, T., & Tao, C. (2020). Progressive dissolution of titanomagnetite in high-temperature hydrothermal vents dramatically reduces magnetization of basaltic ocean crust. *Geophysical Research Letters*, *47*(8), e2020GL087578. https://doi.org/10.1029/2020GL087578

Zhao, X., Housen, B., Solheid, P., & Xu, W. (1998). Magnetic properties of Leg 158 cores: The origin of remanence and its relation to alteration and mineralization of the active TAG mound. In P. M.Herzig, S. E.Humphris, D. J.Miller, & R. A.Zierenberg (Eds.), *Proceedings of the ocean drilling program, scientific results* (Vol. 158, pp. 337–351). https://doi.org/10.2973/odp.proc.sr.158.228.1998

Zhu, Z., Tao, C., Shen, J., Revil, A., Deng, X., Liao, S., et al. (2020). Self-potential tomography of a deep-sea polymetallic sulfide deposit on Southwest Indian Ridge. *Journal of Geophysical Research: Solid Earth*, *125*(11), e2020JB019738. https://doi.org/10.1029/2020JB019738